Hindawi
International Journal of Photoenergy
Volume 2019, Article ID 7183978, 9 pages
https://doi.org/10.1155/2019/7183978

Research Article

Tuning Anatase-Rutile Phase Transition Temperature: TiO_2/SiO_2 Nanoparticles Applied in Dye-Sensitized Solar Cells

Billy N. Cardoso,[1] Emerson C. Kohlrausch,[2] Marina T. Laranjo,[1] Edilson V. Benvenutti,[1] Naira M. Balzaretti,[3] Leliz T. Arenas,[1] Marcos J. L. Santos,[2] and Tania M. H. Costa[1,3]

[1]*Laboratório de Sólidos e Superfícies, Instituto de Química, Universidade Federal do Rio Grande do Sul, 91501–970 Porto Alegre, RS, Brazil*
[2]*Laboratório de Materiais Aplicados e Interfaces, Instituto de Química, Universidade Federal do Rio Grande do Sul, 91501–970 Porto Alegre, RS, Brazil*
[3]*Laboratório de Altas Pressões e Materiais Avançados, Instituto de Física, Universidade Federal do Rio Grande do Sul, 91501–970 Porto Alegre, RS, Brazil*

Correspondence should be addressed to Marcos J. L. Santos; mjls.research@gmail.com
and Tania M. H. Costa; taniahac@gmail.com

Received 1 October 2018; Revised 11 January 2019; Accepted 16 January 2019; Published 13 March 2019

Academic Editor: K. R. Justin Thomas

TiO_2/SiO_2 nanoparticles with 3, 5, and 10 molar percent of silica, were synthesized by hydrothermal method and characterized by SEM, TEM, N_2 adsorption-desorption isotherms, X-ray diffraction, and Raman and UV-Vis spectroscopy. While pristine TiO_2 thermally treated at 500°C presents a surface area of 36 m^2 g^{-1} (±10 m^2 g^{-1}), TiO_2/SiO_2 containing 3, 5, and 10 molar percent of silica present surface areas of 93, 124, and 150 m^2 g^{-1} (±10 m^2 g^{-1}), respectively. SiO_2 is found to form very small amorphous domains well dispersed in the TiO_2 matrix. X-ray diffraction and Raman spectroscopy data show that anatase-to-rutile phase transition temperature is delayed by the presence of SiO_2, enabling single-anatase phase photoanodes for DSSCs. According to the $I \times V$ measurements, photoanodes with 3% of SiO_2 result in improved efficiency, which is mainly related to increased surface area and dye loading. In addition, the results suggest a gain in photocurrent related to the passivation of defects by SiO_2.

1. Introduction

Since the seminal work published by Regan and Graetzel in 1991, DSSCs have been widely studied and have become a broad research field involving semiconductors, organic dyes, inorganic complexes, and electrolytes [1–4]. One of the main components of a DSSC is the nanocrystalline mesoporous photoanode [5]. So far, the most efficient devices are assembled with TiO_2 photoanodes in anatase phase, allowing the fastest charge transfer rates [6, 7]. TiO_2 presents adequate energy gap, high surface area, adequate pore size, high pore volume, nanometric particle size, crystal size, and tunable doping level [8]. Aiming to improve these properties, the development of synthetic approaches to obtain single-anatase phase and shape-controlled TiO_2 nanoparticles is warranted to provide a significant contribution to the field.

The anatase-to-rutile solid-solid phase transition is found to happen in a very wide range of temperatures and is not only dependent on the size of the particles but also on the preparation method, shape of the nanostructure, and presence of dopants and structural defects [9–16]. Indeed, the control over phase formation during the synthesis and the phase transition during thermal treatment are main concerns due to the undesirable formation of the rutile phase at higher temperatures. Aiming to obtain photoanodes assembled with single-anatase phase TiO_2, many works have been developed on the effect of dopants, structural defects, sample preparation, and thermal treatment on TiO_2 [17]. Within this context, SiO_2 is frequently used to control textural, structural,

and morphological properties of TiO_2, improving the efficiency of DSSCs. SiO_2 is mainly applied in the form of particles to increase porosity and to enhance light scattering in TiO_2 photoanodes. Recently, the literature reported the preparation of TiO_2/SiO_2 mixed oxides using the sol-gel method and ball milling to decrease the TiO_2 particle size [6, 9]. In these studies, silica moieties were found to be well dispersed and contributed to maintain the anatase phase even after thermal treatment at 500°C [18–21].

The hydrothermal method is the most used approach to synthesize nanostructured TiO_2 for DSSC. It is a simple and efficient route to obtain a nanosize and shape-controlled TiO_2 nanoparticles and has also been explored to prepare TiO_2/SiO_2 for different applications [10, 22]. In this paper, the main goal is to evaluate the effect of different contents of SiO_2 in a TiO_2 matrix in terms of morphology, surface area, phase transition temperature, and application in DSSC.

2. Materials and Methods

2.1. Materials. Titanium(IV) isopropoxide 97% (TIPOT) (Sigma-Aldrich), tetraethyl orthosilicate 98% (TEOS) (Sigma-Aldrich), absolute ethanol 99% (Synth), isopropyl alcohol 99.5% (Sigma-Aldrich), hydrofluoric acid 40% (HF) (Merck), nitric acid 68% (Sigma-Aldrich), Ruthenizer 535–bisTBA (Solaronix), chloroplatinic acid hexahydrate $\geq 37.50\%$ (Sigma-Aldrich), and Meltonix were obtained from Solaronix.

2.2. Synthesis of TiO_2/SiO_2 Nanopowders. The nanoparticles were synthesized following a previously reported hydrothermal method with modification [19, 23]. In a 0.50 L flask, 0.027 L (0.35 mol) of isopropyl alcohol, 0.030 L (0.1 mol) of TIPOT, and either no TEOS or different amounts of TEOS were added to obtain pristine TiO_2 and TiO_2/SiO_2 with 3, 5, and 10 molar percent of SiO_2. The mixture was maintained at 60°C under constant stirring. 0.160 L of distilled water was added rapidly under vigorous stirring affording a hydrolysis molar ratio $h = (H_2O)/(Ti)$ of 90. After 15 min, 0.0013 L of HNO_3 and 0.0011 L of HF were added as catalysts. The system was maintained under reflux overnight. The samples were washed with absolute ethanol, centrifuged, and dried by evaporation at 60°C for 24 h. The nanoparticles were labelled as S0 (pristine TiO_2), S3 (3% of SiO_2), S5 (5% of SiO_2), and S10 (10% of SiO_2).

2.3. Thermal Treatments. The samples, S0, S3, S5, and S10, were thermally treated at 300, 400, 500, 600, 700, 800, 900, and 1000°C at a heating rate of $5°C \cdot min^{-1}$ for two hours.

2.4. Microscopy Analysis. The morphology was obtained by transmission electron microscopy (TEM) using MET JEM 1200. A small amount of sample was dispersed in isopropyl alcohol using a 450 W ultrasound horn, followed by deposition onto a carbon-coated copper grid.

2.5. UV–Visible Spectroscopy. Diffuse reflectance was performed using a Shimadzu UV–2450PC spectrophotometer with an integrating sphere ISR–2200, at room temperature.

2.6. N_2 Adsorption-Desorption Isotherms. N_2 adsorption-desorption isotherms were determined at the liquid nitrogen boiling point, using a Tristar II 3020 Kr Micromeritics equipment. The samples were previously degassed at 120°C under vacuum, for 12 h. The specific surface areas were determined by the BET (Brunauer, Emmett and Teller) multipoint technique, and the pore size distributions were obtained by using the BJH (Barrett, Joyner, and Halenda) and DFT (Density Functional Theory) methods.

2.7. X-Ray Powder Diffraction (XRD). X-ray powder diffraction (XRD) patterns were obtained using the Siemens D500 diffractometer with Cu–Kα ($\lambda = 1.5418$ Å) in a 2θ range from 10 to 90° with a step size of 0.05° and time of 0.4 s per step.

2.8. Dye-Sensitized Solar Cell Assembly. TiO_2/SiO_2 pastes were screen printed on the transparent conductive substrate (fluorine-doped tin oxide (FTO)) previously soaked in 40 mM $TiCl_4$ aqueous solution at 90°C for 30 minutes. The procedure to obtain the TiO_2/SiO_2 paste can be found elsewhere [24]. The substrate was heated on a hot plate at 125°C for 20 min and at 500°C for 30 min in a tubular oven. The mesoporous TiO_2- (S0) or TiO_2/SiO_2- (S3, S5, and S10) based electrodes were immersed in 0.5 mM cis-bis(isothiocyanato)bis(2,2′–bipyridyl–4,4′–dicarboxylato)–ruthenium(II)—N–719 solution of acetonitrile/tertbutyl alcohol (1 : 1 *v*/*v*) and kept at room temperature 24 h. The counter electrodes were prepared by coating the FTO surface with a 30 μL of 1 mM hexachloroplatinic acid and heated to 400°C. The mediator, responsible for the regeneration of the dye, was placed in between the dye-sensitized photoanode and the counter electrode. The device was sealed using a polymeric film of low melting temperature (Meltonix). The electrolyte was a 0.6 M BMII, 0.03 M I_2, 0.10 M guanidinium thiocyanate, and 0.5 M 4–tertbutyl pyridine in a mixture of acetonitrile and valeronitrile (85 : 15).

2.9. Characterization of the DSSCs. The performance of the DSSCs was evaluated by current versus potential measurements, carried out using the 300 W Xenon arc lamp and the AM1.5 filter. The power of the simulated light was calibrated to 100 mW/cm^2 and recorded by the Keithley picoammeter, model 2400.

3. Results and Discussion

Figure 1 shows the TEM images of the as-synthesized samples and after thermal treatment at 500°C. Before thermal treatment, one can observe dispersed and irregularly shaped nanoparticles with average size smaller than 10 nm (Figures 1(a)–1(d)). After thermal treatment, one can observe the formation of agglomerates. The TEM of S0 (pristine TiO_2) shows the formation nanoparticles with average size larger than 30 nm (Figure 1(e)); meanwhile, the presence of SiO_2 (samples S3, S5, and S10) clearly inhibited nanoparticle growth, resulting in smaller particles with an average size of 10 nm. In the mesoporous photoanodes obtained from these samples (Figure S1), the effect of SiO_2 is also found to result in the formation of smaller agglomerates. EDS

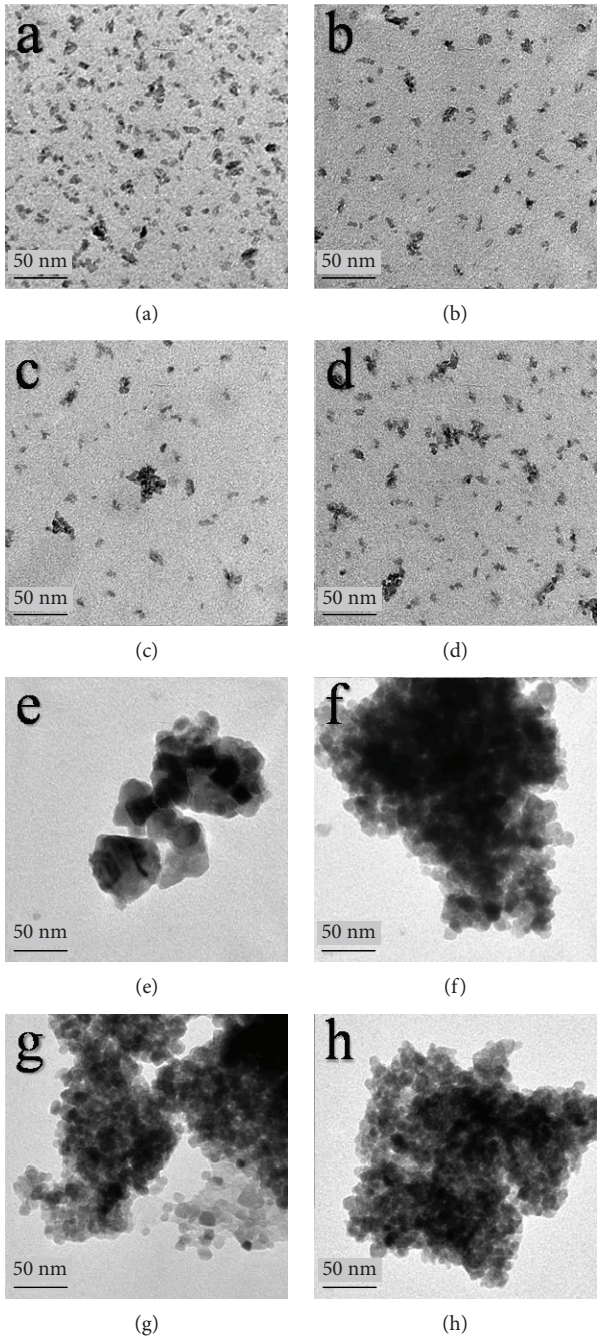

Figure 1: TEM images of S0, S3, S5, and S10 before (a–d) and after (e–h) thermal treatment.

analysis (Table S1) confirms the increase of silica content along with the increasing amount of silica precursor.

N_2 adsorption-desorption isotherms and BJH pore size distribution of the samples thermally treated at 500°C (the same temperature used to prepare the photoanodes for DSSC) are shown in Figures 2(a) and 2(b), respectively. The thermally treated samples were labelled as S0C, S3C, S5C, and S10C. All isotherms are type IV, typical of mesoporous materials with hysteresis in high relative pressures [25]. The hysteresis curves undergo a shift to low pressure with the increase of SiO_2 content changing the mesopore-size distribution profile. While S0C presents large pore-size distribution profile between 10 and 22 nm in diameter, the presence of SiO_2 results in mesopores with sharper distribution and smaller diameters (Figure 2(b)). In very low relative pressures ($P/P_0 < 0.05$), which is related to the micropore region, an increase in amount of adsorbed nitrogen is observed from S0C to S10C. DFT micropore distribution curves, shown in the inset of Figure 2(b), confirm the increase in microporosity produced by the silica moiety.

The surface area and pore volume of the samples are presented in Table 1. As one can observe, pristine TiO_2 (S0C)

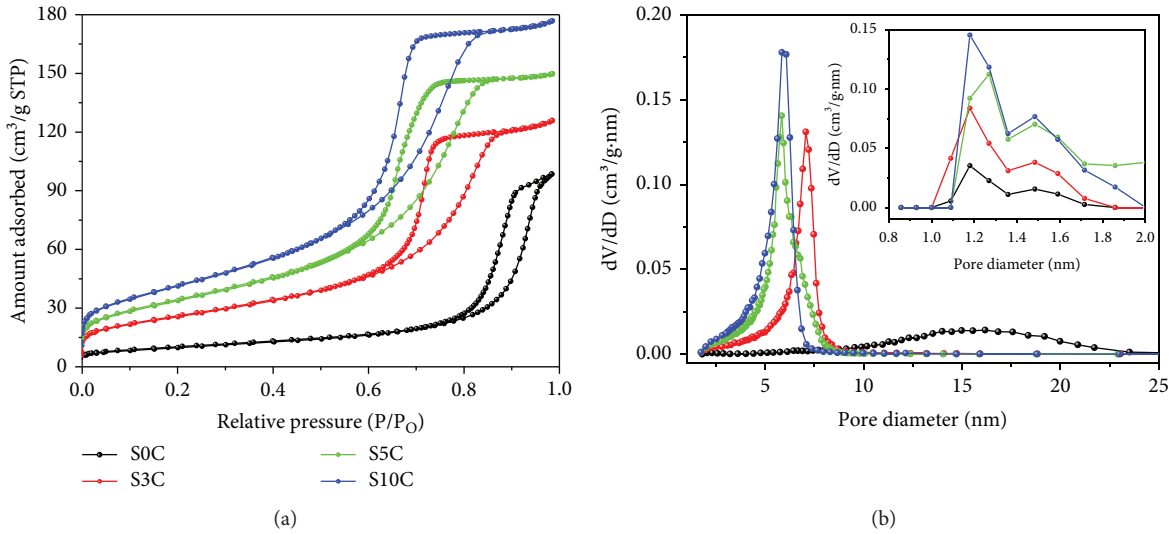

Figure 2: (a) N_2 adsorption-desorption isotherms and (b) BJH pore size distribution of S0C, S3C, S5C, and S10C (thermally treated at 500°C). Inset in (b): the DFT pore size distribution.

Table 1: Surface area and pore volume from the samples thermally treated at 500°C.

Sample	Surface area (m^2g^{-1})	Pore volume (cm^3g^{-1})
S0C	36 ± 3	0.153 ± 0.001
S3C	93 ± 3	0.194 ± 0.001
S5C	124 ± 4	0.233 ± 0.001
S10C	150 ± 4	0.276 ± 0.001

presents a smaller surface area than TiO_2/SiO_2 samples. In addition, the surface area and pore volume is found to increase along with the increase of SiO_2 content, from S3C to S10C. This result corroborates with the literature, indicating that silica affords a surface area to SiO_2/TiO_2 [6]. For S0C, the pore size is related to the agglomeration of large particles, as observed in the TEM images (Figure 1(e)) [9]. For S3C, S5C, and S10C, the average pore diameter 8 nm corroborates with the size of the particles observed by TEM images.

In order to evaluate the influence of SiO_2 content in the anatase-to-rutile phase transition, XRD patterns were obtained from S0, S3, S5, and S10 before and after thermal treatment at 300, 400, 500, 600, 700, 800, 900, and 1000°C (Figure 3). S0 presents diffraction peaks corresponding to the anatase phase (JCPDS# 84-1286) in addition to incipient peaks related to the brookite phase (JCPDS# 29-1360). Anatase-to-rutile phase transition (JCPDS# 76-0649) in the S0 (Figure 3(a)) starts at ca. 400°C, and the complete conversion is observed at temperatures higher than 700°C. Meanwhile, for S3, phase transition only starts at ca. 800°C (Figure 3(b)); for S5 at 900°C (Figure 3(c)) and for S10 at 1000°C (Figure 3(d)). The typical XRD pattern of amorphous SiO_2, which presents a broad peak near 22°, was not observed, strongly suggesting that SiO_2 domains are so small and well dispersed that could not be detected by XRD.

Table 2 shows the change in anatase crystallite size related to the thermal treatment temperature and the SiO_2 content. The crystallite size in S0 was measured as 11 nm at 400°C; meanwhile, in S5 and S10, such crystallite size was only obtained after 700°C. These results show that SiO_2 amorphous domains hinder or delay the grain growth in anatase phase, and this behaviour is more significant for higher concentrations of SiO_2 [9]. Although in S0 the anatase crystallites maintain the size of 11 nm at 500°C, the TEM images (Figure 1) show particles larger than 20 nm for this sample. These results can be explained by the formation of rutile phase after thermal treatment, with crystallite size calculated as 29 nm. The crystallite size exerts a significant influence on the anatase-to-rutile solid–solid phase transition. According to the literature, for this transition to occur, the anatase particles need to grow to a size of approximately 35 nm [26, 27]. Up to this size, the anatase phase has a more stable thermodynamic equilibrium, and the grain grows to decrease the total energy. However, the contribution of bulk energy to total energy increases along with particle size and the anatase phase collapses to decrease the total energy. The transition to the rutile takes place in a reconstructive process, where the Ti–O bonds are ruptured, followed by a structural rearrangement and subsequent formation of new Ti–O bonds in the rutile phase [28, 29]. In this way, the SiO_2 dispersed in the TiO_2/SiO_2 prevented the phase transition by inhibiting the growth of the primary particles [30]. Indeed, these results confirm that a single-anatase phase is obtained even after thermal treatment at 500°C, due to the presence of SiO_2.

Figure 4 shows the Raman spectra of S0, S3, S5, and S10 as synthesized and after thermal treatment at 500°C (as in Figure 2, the samples thermally treated at 500°C are labelled as S0C, S3C, S5C, and S10C). The peaks observed at 163, 406, 514, and 635 cm^{-1} are related to vibrational modes E_g, B_{1g}, A_{1g} or B_{1g}, and E_g, respectively, characteristic of anatase phase (Figure 4(a)). As one can observe, the intensity of these peaks decrease along with the increase in SiO_2 content. According to literature, the strongest E_g mode at

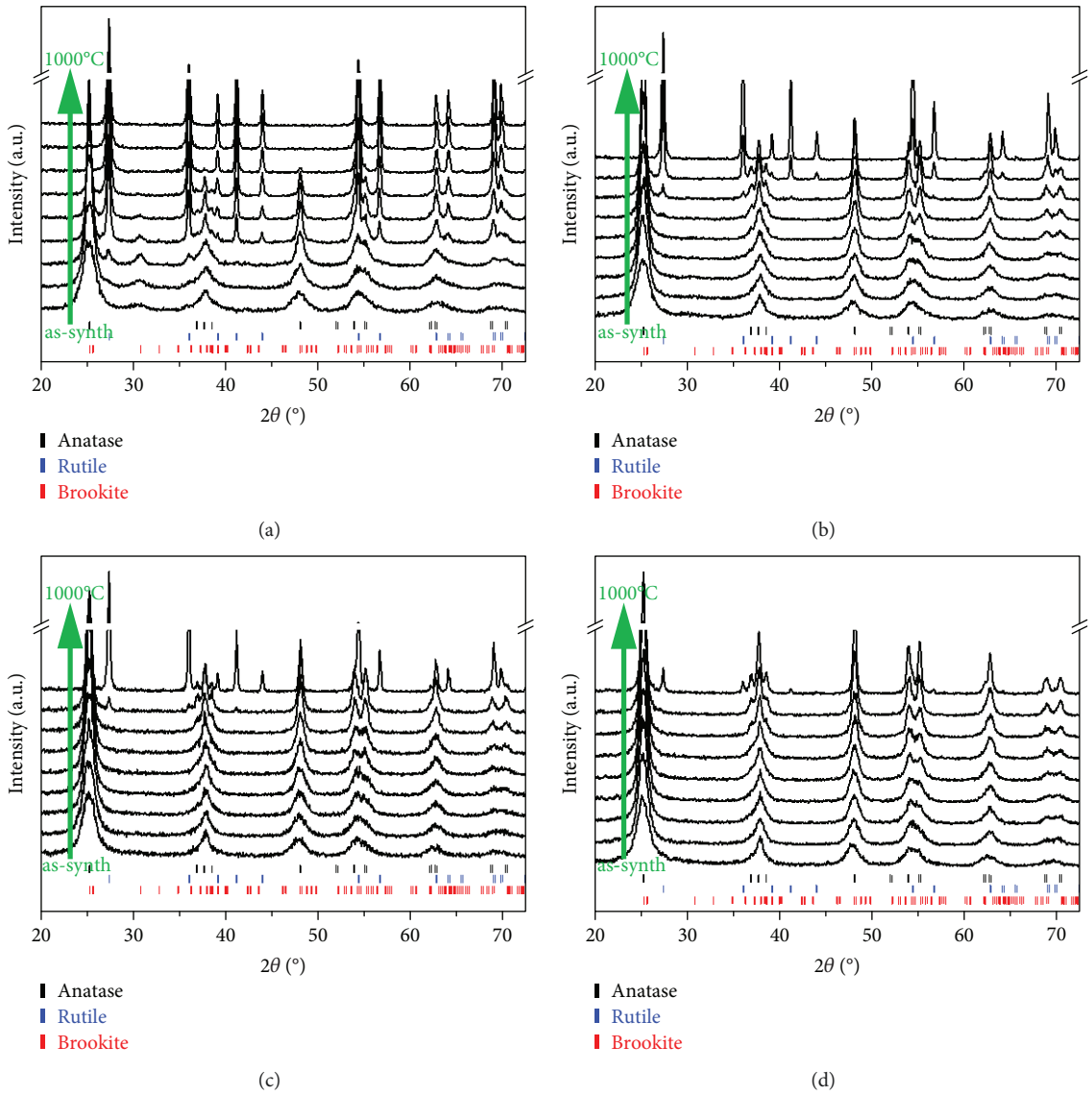

Figure 3: XRD patterns of as-synthesized and thermally treated samples at 300, 400, 500, 600, 700, 800, 900, and 1000°C (a) S0, (b) S3, (c) S5, and (d) S10.

Table 2: Crystallite size for S0, S3, S5, and S10 thermally treated at different temperatures, calculated by using Scherrer's equation.

Temperature (°C)	S0 (nm)	S3 (nm)	S5 (nm)	S10 (nm)
25	6 ± 1	5 ± 1	6 ± 1	5 ± 1
300	8 ± 1	7 ± 1	6 ± 1	8 ± 1
400	11 ± 1	9 ± 1	7 ± 1	9 ± 1
500	11 ± 1	10 ± 1	8 ± 1	9 ± 1
600	—	13 ± 1	9 ± 1	10 ± 1
700	—	16 ± 1	11 ± 1	12 ± 1
800	—	21 ± 1	16 ± 1	13 ± 1
900	—	28 ± 1	21 ± 1	17 ± 1
1000	—	—	—	28 ± 1

163 cm^{-1} is related to the external vibration of the anatase structure, showing that the anatase phase was formed in the as-synthesized TiO_2. After thermal treatment, this peak shifts to lower frequency at 153 cm^{-1}, becoming more well defined and the linewidth decreases [31].

For the S0, the peak characteristic of rutile are observed as a shoulder at 447 cm^{-1} and a peak at 638 cm^{-1}, corresponding to vibrational modes E_g and A_{1g}. Some peaks of rutile and anatase are very similar, such as the ones at 638 and 635 cm^{-1}; therefore, the presence of rutile in the S0C can be identified mainly by the shoulder at 447 cm^{-1} [32]. This shoulder is observed only in S0 corroborating with the early discussion that phase transformation to rutile occurred at 500°C only in the pristine TiO_2. The spectra of S3C, S5C, and S10C are very similar to the spectra of S3, S5, and S10, only showing more well-defined and narrow peaks indicating

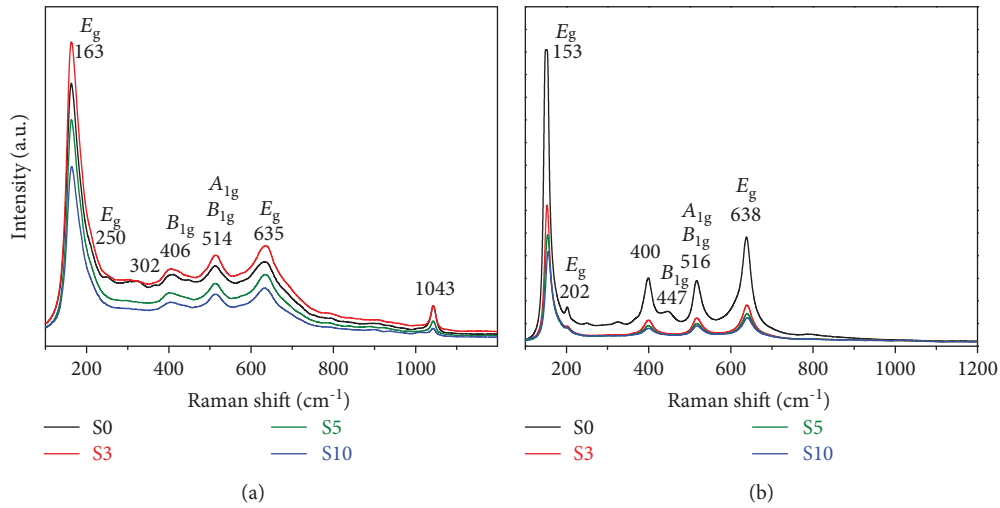

Figure 4: Raman shift of S0, S3, S5, and S10 (a) and S0C, S3C, S5C, and S10C (b).

a better crystallization of anatase in the thermally treated samples (Figure S3).

The UV–visible absorption spectra of as-synthesized and thermally treated samples (Figure S4) present similar optical behavior [33]. The measured reflectance R is not directly proportional to the absorption coefficient, α; so Kubelka-Munk was used to extract α, where $f(R)$ is the Kubelka-Munk function and S is the scattering coefficient,

$$f(R) = \frac{(1-R)^2}{2R} = \frac{\alpha}{S}. \quad (1)$$

By assuming the scattering coefficient to be wavelength independent, $f(R)$ is proportional to α, and the Tauc plots were obtained by plotting $f(R)$ in place of α as a function of the incident radiation energy ($h\nu$), where α is the absorption coefficient and m is equal to 1/2 for a direct gap and 2 for an indirect gap. Extrapolating values of $f(R)$ to zero, the band gap values were determined (Table S2). In general, the band gap values obtained in the present work are similar to the values for TiO_2 earlier described in the literature and were not affected by the presence of the SiO_2 [34, 35]. An interesting result is the tail at around 400 nm decreasing along with the SiO_2 content. Earlier studies have demonstrated that a very thin layer of SiO_2 can passivate defects or trapping states on the TiO_2 surface [36, 37]. Hence, one can suggest that TiO_2 in S3, S5, and S10 presents less defect concentration, which would result in a decrease of charge recombination and improvement of DSSC efficiencies. The spectra of the photoanodes assembled with S0, S3, S5, and S10 and sensitized with the ruthenium complex (Figure S5) show an increase in dye loading depending on the SiO_2 content. The results corroborate with data presented in Table 2, once larger surface areas allow larger dye loading, which ultimately should result in improved photocurrent.

Figure 5 shows the current versus potential curves of the DSSCs assembled with S0C, S3C, S5C, and S10C. The obtained electrical parameters, Fill Factor (FF), and efficiency (η) are described in Table 3. The FF of the devices assembled with S3C, S5C, and S10C presents a slight improvement when compared to S0C. Hence, corroborating with XRD data, the formation of SiO_2 in very small domains does not seem to affect series or parallel resistance of the devices. On the other hand, V_{oc} decreased with the amount of silica. V_{oc} results from the difference between the redox potential of the electrolytes and the quasi-Fermi level of electrons in TiO_2, under illumination. Once the high density of photoexcited electrons can negatively shift the quasi-Fermi level and SiO_2 domains would behave like insulators dispersed into the TiO_2 matrix, we suggest that the presence of result in a small impediment for charge transfer, displacing the quasi-fermi level and resulting in a short open circuit potential [38, 39]. The obtained power conversion efficiencies (at AM 1.5 G illumination) were 2.25%, 3.3%, 2.45%, and 2.1% for the devices based on S0C, S3C, S5C, and S10C, respectively. Therefore, only a small percentage of silica results in some improvement in efficiency, as observed from sample S3.

Figure 6 shows the Nyquist plots of the assembled DSSCs. These plots consist of three components: ohmic resistance R_0 (associated with the series resistance (Rs) of the electrolytes and electrical contacts in the DSSCs), the short arcs (R_1), and the larger arcs (R_2). The arcs in the high frequency (R_1) correspond to the charge–transfer resistance at the Pt counter electrode/electrolyte interface while the arcs at a lower frequency (R_2) are attributed to the charge–transfer resistance at the TiO_2/dye/electrolyte interface. Table 4 summarizes the results obtained by fitting the experimental data, using an equivalent circuit containing a combination of constant phase element (CPE) and resistance components (inset of Figure 6), where CPE_1 and CPE_2 correspond to R_1 and R_2, respectively. These impedances showed an apparent effect on the charge transport in the DSSCs [40–42].

4. Conclusions

Small silica domains dispersed in a TiO_2 matrix were found to delay the temperature of anatase-to-utile phase transition,

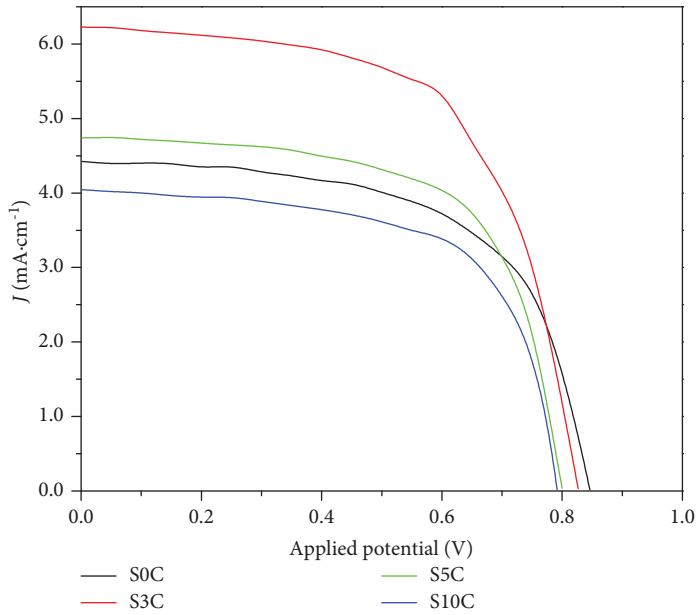

Figure 5: Current versus applied potential curves from DSSCs assembled with S0C, S3C, S5C, and S10C.

Table 3: Electrical parameters of the assembled devices.

Devices	I_{sc} (mA)	V_{oc} (V)	$I_{max}.V_{max}$	FF	n
S0C	4.42	0.85	2.25	60%	2.25%
S3C	6.22	0.84	3.30	63%	3.30%
S5C	4.73	0.81	2.44	64%	2.45%
S10C	4.05	0.80	2.10	65%	2.10%

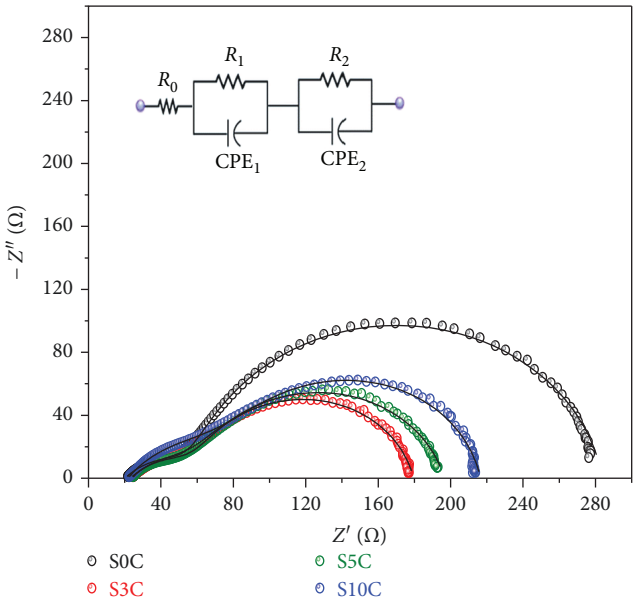

Figure 6: Impedance measurement from DSSCs assembled with S0C, S3C, S5C, and S10C.

to temperatures above the ones usually applied to assemble dye-sensitized solar cells. Hence, more efficient DSSC photoanodes presenting single-anatase phase were obtained. The

Table 4: EIS parameters from the devices determined by fitting the data according to the equivalent circuit model (see Figure 6).

Devices	R_0 (Ω)	R_1 (Ω)	R_2 (Ω)	R_{total} (Ω)
S0C	20.5	42.0	222	284.5
S3C	23.7	46.8	109	179.5
S5C	23.6	39.9	133	196.5
S10C	22.0	68.7	126	216.7

TiO_2/SiO_2 samples present very high surface areas, enabling large dye loading and hence improved photocurrents. The delay in phase transition was related to the inhibition of anatase crystallite growth by the presence of SiO_2. Although all of the samples containing SiO_2 presented larger surface areas than pristine TiO_2, only the photoanodes based on TiO_2/SiO_2 with low concentration of SiO_2 resulted in improved power conversion efficiency.

Data Availability

The data used to support the findings of this study are available from the corresponding author upon request.

Conflicts of Interest

The authors declare that there is no conflict of interest regarding the publication of this paper.

Acknowledgments

The authors are grateful for the financial support from the following Brazilian agencies: Conselho Nacional de Desenvolvimento Científico e Tecnológico, Fundação de Amparo à Pesquisa do Estado do Rio Grande do Sul, and CAPES.

Supplementary Materials

Figure S1: scanning electron microscopy images of (a) S0, (b) S3, (c) S5, and (d) S10. Figure S2: diffraction patterns of the samples (a) before and (b) after thermal treatment at 500°C. Figure S3: Raman Shift of S0, S3, S5, and S10 before and after thermal treatment. Figure S4: direct (left) and indirect (right) Tauc plots for S0, S3, S5, and S10. Figure S5: UV–Visible spectra of S0, S3, S5, and S10 thermally treated at 500°C and sensitized with N-719. Table S1: carbon elemental analysis of the samples. Table S2: direct and indirect band gaps of the samples thermally treated at 500°C. *(Supplementary Materials)*

References

[1] B. O'Regan and M. Graetzel, "A low-cost, high-efficiency solar cell based on dye-sensitized colloidal TiO2 films," *Nature*, vol. 353, p. 737, 1991.

[2] L. M. Peter, "The Grätzel cell: where next?," *Journal of Physical Chemistry Letters*, vol. 2, no. 15, pp. 1861–1867, 2011.

[3] I. Mora-Seró and J. Bisquert, "Breakthroughs in the development of semiconductor-sensitized solar cells," *The Journal of Physical Chemistry Letters*, vol. 1, no. 20, pp. 3046–3052, 2010.

[4] A. Braga, S. Giménez, I. Concina, A. Vomiero, and I. Mora-Seró, "Panchromatic sensitized solar cells based on metal sulfide quantum dots grown directly on nanostructured TiO_2 electrodes," *Journal of Physical Chemistry Letters*, vol. 2, no. 5, pp. 454–460, 2011.

[5] W. Zeng, Y. Cao, Y. Bai et al., "Efficient dye-sensitized solar cells with an organic photosensitizer featuring orderly conjugated ethylenedioxythiophene and dithienosilole blocks," *Chemistry of Matterials*, vol. 22, no. 5, pp. 1915–1925, 2010.

[6] E. C. Kohlrausch, M. J. M. Zapata, R. V. Gonçalves et al., "Polymorphic phase study on nitrogen-doped TiO_2 nanoparticles: effect on oxygen site occupancy, dye sensitized solar cells efficiency and hydrogen production," *RSC Advances*, vol. 5, no. 123, pp. 101276–101286, 2015.

[7] M. S. Ahmad, A. K. Pandey, and N. A. Rahim, "Advancements in the development of TiO_2 photoanodes and its fabrication methods for dye sensitized solar cell (DSSC) applications. A review," *Renewable and Sustainable Energy Reviews*, vol. 77, pp. 89–108, 2017.

[8] C. C. Raj and R. Prasanth, "A critical review of recent developments in nanomaterials for photoelectrodes in dye sensitized solar cells," *Journal of Power Sources*, vol. 317, pp. 120–132, 2016.

[9] H. Zhang and J. F. Banfield, "Understanding polymorphic phase transformation behavior during growth of nanocrystalline aggregates: insights from TiO_2," *The Journal of Physical Chemistry B*, vol. 104, no. 15, pp. 3481–3487, 2000.

[10] M. Pal, J. García Serrano, P. Santiago, and U. Pal, "Size-controlled synthesis of spherical TiO_2 nanoparticles: morphology, crystallization, and phase transition," *Journal of Physical Chemistry C*, vol. 111, no. 1, pp. 96–102, 2007.

[11] H. Zang and J. F. Banfield, "Size dependence of the kinetic rate constant for phase transformation in TiO_2 nanoparticles," *Chemistry of Materials*, vol. 17, no. 13, pp. 3421–3425, 2005.

[12] D. Li, H. Wang, D. Xiao, M. Song, B. Legg, and J. Chun, "Investigating the magnitude and source of orientation-dependent interactions between TiO_2 crystal surfaces," *Nanoscale*, vol. 9, no. 29, pp. 10173–10177, 2017.

[13] D. Majumder and S. Roy, "Non-fluorinated synthesis of anatase TiO_2 with dominant {001} facets: influence of faceted structures on formaldehyde sensitivity," *New Journal of Chemistry*, vol. 41, no. 15, pp. 7591–7597, 2017.

[14] A. Di Paola, G. Marci, L. Palmisanok et al., "Preparation of polycrystalline TiO_2 photocatalysts impregnated with various transition metal ions: characterization and photocatalytic activity for the degradation of 4-nitrophenol," *The Journal of Physical Chemistry B*, vol. 106, no. 3, pp. 637–645, 2002.

[15] A. Fuerte, M. D. Hernández-Alonso, A. J. Maira et al., "Visible light-activated nanosized doped-TiO_2 photocatalysts," *Chemical Communications*, vol. 33, no. 24, pp. 2718-2719, 2001.

[16] R. Asahi, T. Morikawa, T. Ohwaki, K. Aoki, and Y. Taga, "Visible-light photocatalysis in nitrogen-doped titanium oxides," *Science*, vol. 293, no. 5528, pp. 269–271, 2001.

[17] M. K. Hossain, M. F. Pervez, M. N. H. Mia et al., "Annealing temperature effect on structural, morphological and optical parameters of mesoporous TiO_2 film photoanode for dye-sensitized solar cell application," *Materials Science-Poland*, vol. 35, no. 4, pp. 868–877, 2018.

[18] M. T. Laranjo, N. C. Ricardi, L. T. Arenas et al., "TiO_2 and TiO_2/SiO_2 nanoparticles obtained by sol–gel method and applied on dye sensitized solar cells," *Journal of Sol-Gel Science and Technology*, vol. 72, no. 2, pp. 273–281, 2014.

[19] S. Murali, S. P. Lee, and D. P. Birnie III, "The importance of silica morphology in silica–titania composites with dye sensitized solar functionality," *Thin Solid Films*, vol. 537, pp. 80–84, 2013.

[20] K.-H. Park, H.-B. Gu, E. M. Jin, and M. Dhayal, "Using hybrid silica-conjugated TiO_2 nanostructures to enhance the efficiency of dye-sensitized solar cells," *Electrochimica Acta*, vol. 55, no. 19, pp. 5499–5505, 2010.

[21] M. T. Laranjo, N. C. Ricardi, L. T. Arenas et al., "Influence of ball milling on textural and morphological properties of TiO_2 and TiO_2/SiO_2 xerogel powders applied in photoanodes for solar cells," *Journal of Solid State Electrochemistry*, vol. 20, no. 6, pp. 1731–1741, 2016.

[22] C. Gaidau, A. Petica, M. Ignat et al., "Preparation of silica doped titania nanoparticles with thermal stability and photocatalytic properties and their application for leather surface functionalization," *Arabian Journal of Chemistry*, vol. 10, no. 7, pp. 985–1000, 2017.

[23] R. Bleta, A. Lannoy, C. Machut, E. Monflier, and A. Ponchel, "Understanding the role of cyclodextrins in the self-assembly, crystallinity, and porosity of titania nanostructures," *Langmuir*, vol. 30, no. 39, pp. 11812–11822, 2014.

[24] S. Ito, T. N. Murakami, P. Comte et al., "Fabrication of thin film dye sensitized solar cells with solar to electric power conversion efficiency over 10%," *Thin Solid Films*, vol. 516, no. 14, pp. 4613–4619, 2008.

[25] E. V. Benvenutti, C. C. Moro, T. M. H. Costa, and M. R. Gallas, "Materiais híbridos à base de sílica obtidos pelo método sol-gel," *Química Nova*, vol. 32, no. 7, pp. 1926–1933, 2009.

[26] A. A. Gribb and J. F. Banfield, "Particle size effects on transformation kinetics and phase stability in nanocrystalline TiO_2," *American Mineralogist*, vol. 82, no. 7-8, pp. 717–728, 1997.

[27] H. Zhang, B. Chen, and J. F. Banfield, "The size dependence of the surface free energy of titania nanocrystals," *Physical Chemistry Chemical Physics*, vol. 11, no. 14, pp. 2553–2558, 2009.

[28] S. H. Tolbert and A. P. Alivisatos, "Size dependence of a first order solid–solid phase transition: the wurtzite to rock salt transformation in CdSe nanocrystals," *Science*, vol. 265, no. 5170, pp. 373–376, 1994.

[29] K. Jacobs, D. Zaziski, E. C. Scher, A. B. Herhold, and A. P. Alivisatos, "Activation volumes for solid-solid transformations in nanocrystals," *Science*, vol. 293, no. 5536, pp. 1803–1806, 2001.

[30] H. Chang, S. K. Kim, H. D. Jang, and S. W. Cho, "Effect of SiO_2 nanoparticles on the phase transformation of TiO_2 in micron-sized porous TiO_2–SiO_2 mixed particles," *Materials Letters*, vol. 65, no. 21-22, pp. 3272–3274, 2011.

[31] W. F. Zhang, Y. L. He, M. S. Zhang, Z. Yin, and Q. Chen, "Raman scattering study on anatase TiO_2 nanocrystals," *Journal of Physics D: Applied Physics*, vol. 33, no. 8, pp. 912–916, 2000.

[32] K. A. Smith, A. I. Savva, Y. Wu et al., "Effects of intermediate energy heavy–ion irradiation on the microstructure of rutile TiO_2 single crystal," *Journal of the American Ceramic Society*, vol. 101, no. 9, pp. 4357–4366, 2018.

[33] J. Zhang, P. Zhou, J. Liu, and J. Yu, "New understanding of the difference of photocatalytic activity among anatase, rutile and brookite TiO2," *Physical Chemistry Chemical Physics*, vol. 16, no. 38, pp. 20382–20386, 2014.

[34] S. J. Darzi, A. R. Mahjoub, and A. Hosseinian, "Structural, optical and photocatalytic properties of sol–gel synthesized mesoporous TiO_2 film," *Journal of Nanoscience and Nanotechnology*, vol. 10, no. 9, pp. 6099–6103, 2010.

[35] M. K. Nazeeruddin, E. Baranoff, and M. Grätzel, "Dye-sensitized solar cells: a brief overview," *Solar Energy*, vol. 85, no. 6, pp. 1172–1178, 2011.

[36] V. Saxena and D. K. Aswal, "Surface modifications of photoanodes in dye sensitized solar cells: enhanced light harvesting and reduced recombination," *Semiconductor Science and Technology*, vol. 30, no. 6, article 064005, 2015.

[37] S. Yuan, Q. Tang, B. He, L. Men, and H. Chen, "Transmission enhanced photoanodes for efficient dye-sensitized solar cells," *Electrochimica Acta*, vol. 125, no. 10, pp. 646–651, 2014.

[38] P. K. Nayak, J. Bisquert, and D. Cahen, "Assessing possibilities and limits for solar cells," *Advanced Materials*, vol. 23, no. 25, pp. 2870–2876, 2011.

[39] P. Xu, Q. Tang, B. He, Q. Li, and H. Chen, "Transmission booster from SiO_2 incorporated TiO_2 crystallites: enhanced conversion efficiency in dye-sensitized solar cells," *Electrochimica Acta*, vol. 134, no. 10, pp. 281–286, 2014.

[40] S. Sarker, A. J. S. Ahammad, H. W. Seo, and D. M. Kim, "Electrochemical impedance spectra of dye-sensitized solar cells: fundamentals and spreadsheet calculation," *International Journal of Photoenergy*, vol. 2014, Article ID 851705, 17 pages, 2014.

[41] A. Sacco, "Electrochemical impedance spectroscopy: fundamentals and application in dye-sensitized solar cells," *Renewable and Sustainable Energy Reviews*, vol. 79, pp. 814–829, 2017.

[42] P. Bhatt, K. Pandey, P. Yadav, B. Tripathi, and M. Kumar, "Impedance spectroscopic investigation of the degraded dye-sensitized solar cell due to ageing," *International Journal of Photoenergy*, vol. 2016, Article ID 8523150, 9 pages, 2016.